Advances in Aircraft and Spacecraft Science, *Vol. 12, No. 3 (2025) 269-290*
https://doi.org/10.12989/aas.2025.12.3.269

A low-thrust efficient strategy for orbit circularization of small satellites

Khouane Boulanouar*[1], Bekhadda Nacera[2] and Benmansour J. Eddine[2]

[1]*Department of Mission and Space Systems, Satellite Development Center, BP 4065, Ibn Rochd USTO, Oran, 31130, Algeria*
[2]*Department of Space Mechanics Research, Satellite Development Center, BP 4065, Ibn Rochd USTO, Oran, 31130, Algeria*

(Received April 3, 2024, Revised July 31, 2025, Accepted August 23, 2025)

Abstract. Low-thrust propulsion strategies for orbit circularization of small satellites have gained significant attention in recent years due to their potential to reduce propellant consumption and improve maneuverability. This study investigates the application of continuous low-thrust propulsion for achieving orbit circularization in small satellites. The spacecraft's dynamics are modeled using the Lagrange Planetary Equations, and an optimal control law is developed based on a Hamiltonian formulation. The control strategy includes optimal thrust integration, targeting changes in both the semi-major axis and eccentricity. The proposed control law is validated through high-fidelity numerical simulations using STK Astrogator. Propagation is carried out with the High Precision Orbit Propagator (HPOP), which accounts for realistic environmental disturbances. The simulation results demonstrate that the designed low-thrust strategy effectively reduces both maneuver time and the required propellant while achieving successful orbit circularization. This work contributes to the development of efficient, accurate, and operationally feasible low-thrust guidance techniques for future small satellite missions.

Keywords: electric propulsion; space missions; high-precision orbit propagator; Lagrange planetary equations; low-thrust propulsion; spacecraft orbit

1. Introduction

Electric propulsion (EP) orbit maneuvers have become essential in recent years for space exploration and mission design (Krejci and Lozano 2018, Morante and Sanjurjo 2021). This growing importance stems from their superior precision, fuel efficiency, and cost-effectiveness compared to traditional high-thrust maneuvers. Specifically, EP's high exhaust velocity and continuous thrust enable precise control of a spacecraft's trajectory and orbital parameters, making these systems particularly reliable for orbit-to-body transfers and satellite orbit insertion in geocentric trajectories. Despite these advantages, designing optimal transfer trajectories for EP-based missions, particularly in the near-Earth region, remains challenging due to prolonged transfer times and multiple orbital revolutions, which contrast sharply with the rapid maneuvers enabled by chemical propulsion. Nevertheless, low-thrust systems have revolutionized mission planning by enabling precise satellite deployment, spacecraft relocation, and rendezvous

*Corresponding author, Associate Professor, E-mail: b.khouane@gmail.com

http://www.techno-press.org/?journal=aas&subpage=7 ISSN: 2287-528X (Print), 2287-5271 (Online)

operations with unprecedented control and accuracy. Additionally, their superior fuel efficiency reduces emissions and operational costs, making them indispensable tools for modern space missions.

Low-thrust circularization orbits are orbit maneuvers that use low-thrust propulsion to transition from an elliptical orbit to a nearly circular one. This approach offers substantial fuel and time savings by reducing the orbit's energy and the delta-V requirements of the mission (Yue *et al.* 2009). These systems, such as ion and electrospray thrusters, provide continuous force for precise orbital adjustments with minimal propellant consumption (Marcuccio *et al.* 2015, Misuri *et al.* 2015). Due to their high specific impulse, they are ideal for missions where mass and power constraints rule out chemical propulsion, especially on small satellites (Miller *et al.* 2020). For example, ion thrusters excel in high delta-V scenarios, such as deep-space travel, while electrospray devices are optimized for low-impulse, long-duration tasks, such as station-keeping. Such efficiency has been demonstrated in missions like Deep Space 1, where ion propulsion enabled extended operations with limited fuel (Rayman *et al.* 2000, Manzella 2014).

The theoretical foundation for these trajectories has been studied by many scientists, including Edelbaum (Casalino and Colasurdo 2007), who was among the first to demonstrate the advantages of low-thrust propulsion in space missions. Building on this foundation**,** researchers such as Petropoulos (2003, 2004), Betts and Erb (2003), Kéchichian (2017) have made significant contributions that have advanced our understanding of low-thrust trajectory optimization.

Optimizing low-thrust trajectories can be done using a variety of approaches, including direct methods (Enright and Conway 1999, Herman and Spencer 2002), indirect methods (Kechichian 1997, Haberkorn and Gergaud 2004), and heuristic methods (Sentinella and Casalino 2006, Vavrina and Howell 2009). These methods can be used alone or in combination, depending on the specific problem being solved. The first method directly solves the optimization problem. This can be achieved using various numerical optimization techniques, including gradient descent and genetic algorithms. The second method transforms the optimization problem into a simpler form that can be solved more easily. This is often done by employing a variational approach, which reformulates the optimization problem into a differential equation that can be solved using numerical methods. The third method employs trial-and-error techniques to identify practical solutions. A minimum-time guidance problem for low-thrust geostationary transfer orbit (GTO) to geostationary Earth orbit (GEO) transfers was solved by Han *et al.* (2020) using linearized state equations expressed in terms of the angular momentum vector and the eccentricity vector. Taheri *et al.* (2017) have developed a co-state initialization method for the TPBVP (indirect optimization) in minimum-time low-thrust trajectory optimization using shape-based approximations. The performance of the approach for two interplanetary rendezvous missions from Earth to Mars and from Earth to asteroid Dionysus. An indirect optimization approach for low-thrust Earth orbit transfers has been proposed by Wang *et al.* (2021), utilizing nonsingular vectorial orbital elements and co-state parameter estimation to solve the TPBVP. The variety of available approaches to low-thrust trajectory optimization is necessary because different approaches are better suited for different types of problems. For an excellent overview of these methods, refer to Rao (2009) and Conway (2012). The authors provide a comprehensive overview of various trajectory optimization approaches, along with illustrative examples of their application. With the growing demand for efficient and cost-effective space missions, there is an increasing need for advanced methods in orbital transfer planning. Conventional trajectory optimization techniques particularly those applied to low-thrust propulsion systems have often been formulated using indirect methods (e.g., Kechichian 1997, Haberkorn and Gergaud 2004, Taheri *et al.* 2017, Han *et al.* 2020, Wang *et al.*

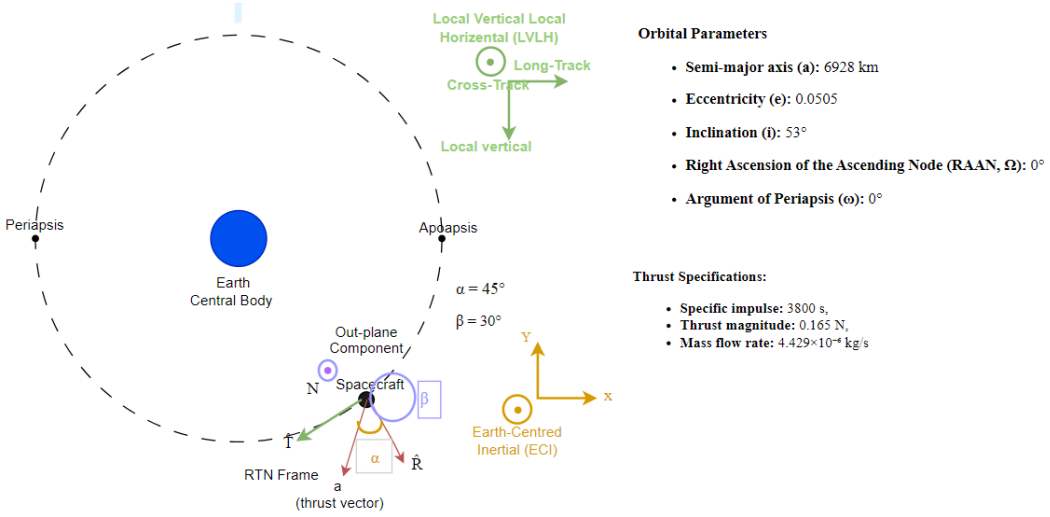

Fig. 1 Spacecraft orbital dynamics-RTN coordinate system with low-thrust vector orientation (azimuth α and elevation β angles in RTN reference frame) (Reiter and Spencer 2016)

2021, Herman *et al.* 2002). However, many of these approaches overlook the impact of space environment perturbations, such as atmospheric drag, solar radiation pressure, and non-spherical gravity, which can significantly affect long-duration, low-thrust maneuvers. These perturbations, such as gravitational forces from celestial bodies and atmospheric drag, can significantly impact the accuracy and efficiency of orbital transfers. To address this issue, the Lagrange planetary equations and the STK AGI software can be used to model low-thrust circularization orbits accurately.

The Lagrange planetary equations are a set of equations used to calculate the motion of planets and other celestial bodies in space. At the same time, the STK AGI software is a powerful tool that can simulate and analyze spacecraft trajectories (AGI 2008). Specifically, the low thrust circularization orbit is scenario is conducted within an integrated STK module called an Astrogator, which employs advanced precise propagators such as the HPOP, which can incorporate multiple perturbing factors such as space environmental effects, including central body gravity, solar radiation pressure, atmospheric drag model, and third body gravity. Through this integrated approach, the proposed method aims to enhance the accuracy and reliability of orbital transfer planning for low-thrust propulsion systems in complex space environments. These two tools can be used in conjunction to model low-thrust circularization orbits and accurately optimize mission plans.

This paper investigates low-thrust orbital circularization strategies for small satellites operating in low Earth orbit (LEO), aiming to enhance mission efficiency through advanced orbital mechanics and high-fidelity simulations. The analysis begins with the formulation of spacecraft dynamics using the Gauss form of the Lagrange Planetary Equations (LPE), providing a rigorous foundation for modeling continuous low-thrust propulsion in the radial–transverse–normal (RTN) frame. For validation, the analytically derived thrust control law was implemented in STK Astrogator using a finite maneuver. propagation was performed using the HPOP, which includes a comprehensive set of perturbative forces. Although the control law was originally designed under a two-body formulation, it was successfully applied within the HPOP environment. For each

maneuver segment, optimal thrust directions were computed and applied to reduce both the semi-major axis and eccentricity, enabling the realistic execution of the analytical strategy under perturbed conditions. Finally, the simulation results confirm the effectiveness of electric propulsion and the optimal control approach for achieving gradual orbit circularization over a 5-day low-thrust maneuver.

2. Satellite trajectory design using thrusting laws for orbital element correction

The optimization of low-thrust trajectories involves determining a control law that defines both the thrust magnitude and direction, as well as the transfer orbit. This process aims to minimize a performance index, such as propellant mass or time of flight, while satisfying the boundary conditions for departure and arrival orbits. In this study, we consider the satellite to be subject to a low-thrust acceleration denoted by $\boldsymbol{f_{th}}$, which can be conveniently expressed in a RTN reference frame as described in Vallado (2001) and Fig. 1. The accelerations due to the thruster are given by the equation below.

$$\boldsymbol{f_{th}} = \begin{bmatrix} f_{\mathrm{R}} \\ f_{\mathrm{T}} \\ f_{\mathrm{N}} \end{bmatrix} = \chi \begin{bmatrix} \cos\beta \sin\alpha \\ \cos\beta \cos\alpha \\ \sin\beta \end{bmatrix} \tag{1}$$

where χ represents the constant magnitude of the low-thrust acceleration, while the thrust pointing angle corresponding to the direction within the instantaneous orbit plane is denoted by α, and the angle β is the angle that defines the out-of-plane thrust component. f_R, f_T, and f_N are the three components of the propulsive acceleration vector projected onto the tangential-normal coordinate frame (as shown in Fig. 1). Gauss's equations describe how the osculating classical orbital elements change over time due to the low-thrust acceleration $\boldsymbol{f_{th}}$. We employ a low-thrust trajectory model, known as nuclear electric propulsion (NEP), to achieve this study.

3. Gauss' equations for the time variation of orbital elements

Gauss's equations describe the time variation of the osculating classical orbital elements resulting from low-thrust acceleration $\boldsymbol{f_{th}}$. When we substitute the expression from Eq. (1) into the Gauss form Battin (1999) of the LPE, we obtain the following

$$\frac{da}{dt} = \frac{2a^2}{h}\chi\cos\beta\left[e\sin\theta\sin\alpha + \frac{p}{r}\cos\alpha\right],$$

$$\frac{de}{dt} = \chi\frac{\cos\beta}{h}\left\{p\sin\theta\sin\alpha + \left[(p+r)\cos\theta + re\right]\cos\alpha\right\},$$

$$\frac{di}{dt} = \chi\frac{r}{h}\cos\upsilon\sin\beta,$$

$$\frac{d\Omega}{dt} = \chi\frac{r\sin\upsilon}{h\sin i}\sin\beta,$$

$$\frac{d\omega}{dt} = \frac{1}{he}\chi\cos\beta\left[-p\cos\theta\sin\alpha + (p+r)\sin\theta\cos\alpha\right] - \frac{r\sin\upsilon\cos i}{h\sin i}\sin\beta,$$

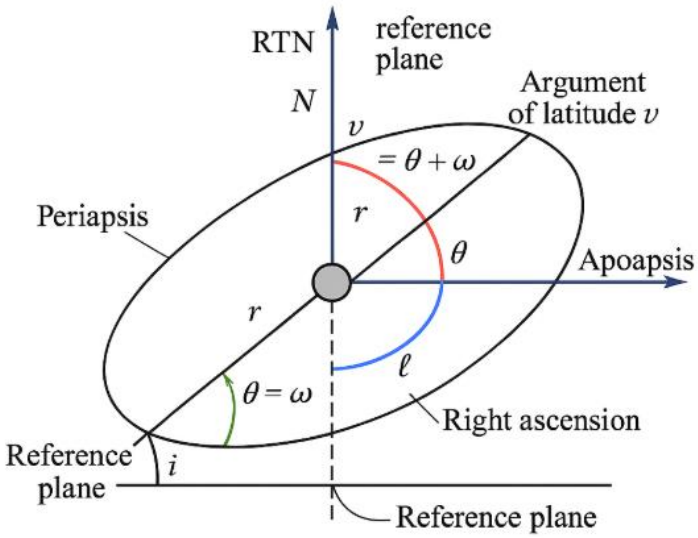

Fig. 2 Orbital elements and reference coordinate system

$$\frac{d\theta}{dt} = \frac{h}{r^2} + \frac{\chi}{eh}\cos\beta\left[p\cos\theta\sin\alpha - (p+r)\sin\theta\cos\alpha\right] \approx \frac{h}{r^2} \tag{2}$$

where a is the semi-major axis, p is the semi-latus rectum, e is the eccentricity, Ω is right ascension of the ascending node, i is the inclination, h is the magnitude of the angular momentum, ω is the argument of periapsis, θ is the true anomaly, r is the orbital radius, υ is the argument of latitude, and $\frac{h}{r^2}$ is the Keplerian rate of true anomaly. Fig. 2 illustrates the orbital parameters and reference frame used in the manuscript.

4. Performance evaluation of the NEP spacecraft thruster

The performance of the NEP spacecraft thruster depends on several factors (Betancourt *et al.* 2021), including the design of the EP spacecraft, which incorporates principles of mechanics, thermodynamics, and nuclear technology, as well as factors like payloads and mission duration. The effectiveness of an electric propulsion system is influenced by several key parameters, including specific impulse, lifetime, and thrust efficiency (O'Reilly 2021, Miao *et al.* 2022).

4.1 Specific impulse

The specific impulse I_{sp} represents the impulse per unit weight of propellant. It indicates the efficiency of a propulsion system and is usually measured at sea level, depending on the engine's operating environment. Assuming a constant thrust and propellant mass flow rate, I_{sp} is expressed as

$$I_{sp} = \frac{F_{th}}{\dot{m}g_0} = \frac{V_E}{g_0} \tag{3}$$

where F_{th} represents the thrust force, $\dot{m}$ denotes the propellant mass flow rate, V_E is the exhaust velocity of the thruster, and g_0 represents the standard gravitational acceleration, which has a value of 9.80665 m/s^2.

4.2 Thrust efficiency

The thrust efficiency is the ratio of the kinetic power used for thrust to the electrical power supplied to the thruster.

$$\eta_{EP} = \frac{\frac{1}{2}\dot{m}V_E^{\,2}}{P_{EP}} \tag{4}$$

where P_{EP} refers to the input electrical power, while the efficiency of the electrical propulsion thruster is represented by the symbol η_{EP}.

4.3 Lifetime

The lifetime of a satellite using EP depends on the mission duration, available propellant, and the total acceleration the propulsion system can provide. To assess mission feasibility and propulsion needs, the Tsiolkovsky rocket equation is often used to estimate the total ΔV required for a specific maneuver.

$$\Delta V = I_{sp} \cdot g_0 \cdot \ln\left(\frac{M_i}{M_f}\right) \tag{5}$$

where M_i is the initial mass, and M_f is the final mass.

The initial mass of a satellite can be calculated by adding up its main subsystems, including the propellant mass, payload mass, power system mass, and structural mass, as shown in the following equation

$$M_i = M_p + M_{PL} + M_W + M_S \tag{6}$$

where the propellant mass is represented by M_p, while M_{PL} refers to the payload mass used by the satellite, the dry mass of the power source is denoted by M_W, and M_S represents the structural mass. The trajectory characteristic is described by $\Im$ which is expressed as

$$\Im = \frac{1}{2}\int_0^{t_f} \frac{\chi^2 \eta_{EP}}{\dot{m}P_{EP}} dt \tag{7}$$

Assuming constant thrust χ, the expression simplifies to

$$\begin{aligned} \Im &= \frac{1}{2}\frac{\chi^2}{\dot{m}}\frac{\eta_{EP}}{P_{EP}}\int_0^{t_f} dt \\ &= \frac{1}{2}\cdot\frac{\chi^2}{\dot{m}}\frac{\eta_{EP}}{P_{EP}}\cdot t_f \end{aligned} \tag{8}$$

Solving for the propellant mass M_p, we obtain

$$M_p = \frac{\Im P_{EP}}{\eta_{EP} I_{sp} g_0} \tag{9}$$

$$M_P = \frac{2P_{EP} \cdot t_f \cdot \eta_{EP}}{V_E^{\,2}} \tag{10}$$

In EP, we have

$$P_{EP} t_f \eta_{EP} = \frac{1}{2} M_P V_E^{\,2} \tag{11}$$

Then

$$M_P = \frac{2P_{EP} t_f \eta_{EP}}{\left(I_{sp} \cdot g_0\right)^2} = \frac{4 \cdot P_{EP}^{\,2} \cdot \dot{m} \cdot \Im}{\chi^2 \cdot V_E^{\,2}} \tag{12}$$

To determine the optimal thrusting laws, the expressions from Eq. (1) are substituted into the Gauss form of the LPE (Eq. (2)). This allows for identification of thrust directions and magnitudes that efficiently achieve the desired changes in the orbital elements.

5. Necessary conditions for optimal control in minimum-time transfers

To optimize a continuous low-thrust trajectory for minimum time, the control strategy must minimize the thrust duration while achieving an orbital maneuver that drives the eccentricity toward zero, resulting in a circularized orbit. Although fuel consumption is inherently linked to thrust duration, the primary objective in this case is to reduce the time of flight t_f. Accordingly, the thrust profile is formulated to maximize acceleration efficiency and achieve rapid circularization within the system's operational limits. The optimization of low-thrust trajectories is modelled as an optimal control problem, which is formulated as follows

$$J = \int_{t_0}^{t_f} dt = t_f - t_0 \tag{13}$$

where J is the cost function representing the total time of flight, where the purpose is to minimize the total maneuver duration from initial time t_0 to final time t_f. Thus, the state vector $\boldsymbol{x} = [a, e, i, \Omega, \omega, \theta]^T$ is used to represent the spacecraft's osculating orbital elements. The expressions of Eq. (2) in the Gauss form of the LPE can be represented as

$$\dot{x}\left(t\right) = \mathbf{F}\left(x, t\right)\boldsymbol{u} + f \tag{14}$$

where

$$\mathbf{F}(x,t)=\chi\begin{bmatrix} \frac{2a^2 e\sin\theta}{h} & \frac{2a^2}{h}\frac{p}{r} & 0 \\ \frac{p\sin(\theta)}{h} & \frac{(p+r)\cos\theta+re}{h} & 0 \\ 0 & 0 & \frac{r}{h}\cos\upsilon \\ 0 & 0 & \frac{r\sin\upsilon}{h\sin i} \\ -\frac{p\cos\theta}{he} & \frac{(p+r)\sin\theta}{he} & -\frac{r\sin\upsilon\cos i}{h\sin i} \\ \frac{p\cos\theta}{eh} & -\frac{(p+r)\sin\theta}{eh} & 0 \end{bmatrix},\quad \boldsymbol{f}=\begin{bmatrix} 0 \\ 0 \\ 0 \\ 0 \\ 0 \\ \frac{h}{r^2} \end{bmatrix},$$

$\chi=\frac{T_{\max}}{m}$, $T_{\max}$ is the maximum thrust amplitude available, m represents the instantaneous mass of the spacecraft, and $\boldsymbol{f}$ represents the uncontrollable Keplerian motion.

In our two-body control system model, where no perturbing forces act except for the control thrust, the disturbing acceleration vector $\boldsymbol{f_{th}}$ comes only from the propulsion system, as presented in Eq. (1).

$$\boldsymbol{f}_{th}=\frac{T_{\max}}{m}\boldsymbol{u} \tag{15}$$

The mass flow rate of propellant consumption is governed by the thrust magnitude and specific impulse, where the instantaneous mass depletion relates to the throttle setting $|\boldsymbol{u}(t)|$ through

$$\dot{m}(t)=-\frac{T(t)}{I_{sp}g_0}=-\frac{T_{\max}}{I_{sp}}\frac{|\boldsymbol{u}(t)|}{g_0} \tag{16}$$

where $T(t)=\boldsymbol{T_{max}}|\boldsymbol{u}(\boldsymbol{t})|$, $\boldsymbol{u}(\boldsymbol{t})$ is given by

$$0\le|\boldsymbol{u}(t)|\le 1 \tag{17}$$

The Hamiltonian function is defined as

$$H=1+\boldsymbol{\lambda}_{\mathbf{x}}^{T}\dot{\boldsymbol{x}}+\lambda_m\dot{\boldsymbol{m}} \tag{18}$$

where $\boldsymbol{\lambda_x}$ represents the costate vector associated with the state vector $\boldsymbol{x}$, while λ_m denotes the co-state variable related to the mass dynamics.

Substituting $\dot{\boldsymbol{x}}$ and $\dot{m}$

$$H=1+\boldsymbol{\lambda}_x^T\left(\mathbf{F}(x,t)\mathbf{u}+\boldsymbol{f}\right)+\lambda_m\left(-\frac{T_{\max}}{I_{sp}g_0}|\boldsymbol{u}|\right) \tag{19}$$

By simplifying Eq. (19), we obtain

$$H=1+\boldsymbol{\lambda}_x^T\boldsymbol{f}+\left(\boldsymbol{\lambda}_x^T\mathbf{F}(x,t)-\frac{\lambda_m m}{I_{sp}g_0}\right)\boldsymbol{u} \tag{20}$$

Based on refs (Wang *et al*. 2021, Ma *et al*. 2021), the governing differential equations of costate variables were derived directly, thus allowing for the omission of specific derivation processes.

5.1 Derivation of costate dynamics

Pontryagin's Maximum Principle states that the costates evolve as

$$\dot{\boldsymbol{\lambda}}_{\boldsymbol{x}} = -\left(\frac{\partial H}{\partial \boldsymbol{x}}\right)^T \tag{21}$$

Expand the Hamiltonian's partial derivative

$$\frac{\partial H}{\partial \boldsymbol{x}} = \frac{\partial}{\partial \boldsymbol{x}}\left(1 + \boldsymbol{\lambda}_x^T \boldsymbol{F}\left(x,t\right)\boldsymbol{u} + \boldsymbol{\lambda}_x^T \boldsymbol{f} - \lambda_m \frac{T_{\max}}{I_{sp} g_0}|\boldsymbol{u}|\right) \tag{22}$$

Since 1 and $|\boldsymbol{u}|$ are independent of $\boldsymbol{x}$, this simplifies to

$$\frac{\partial H}{\partial \boldsymbol{x}} = \boldsymbol{u}^T \frac{\partial}{\partial \boldsymbol{x}}\left(\boldsymbol{F}\left(x,t\right)\boldsymbol{\lambda}_x\right) + \frac{\partial}{\partial \boldsymbol{x}}\left(\boldsymbol{\lambda}_x^T \boldsymbol{f}\right) \tag{23}$$

The term $\boldsymbol{F}(x,t)\boldsymbol{\lambda}_x$ is a vector. Its derivative with respect to $\boldsymbol{x}$ is a Jacobian matrix and the term $\boldsymbol{f}$ represents Keplerian motion. Accordingly, the costate dynamics become as

$$\dot{\boldsymbol{\lambda}}_x = -\left[\boldsymbol{u}^T\left(\frac{\partial \boldsymbol{F}}{\partial \boldsymbol{x}}\right)^T \boldsymbol{\lambda}_x + \boldsymbol{\lambda}_x^T \frac{\partial \boldsymbol{f}}{\partial \boldsymbol{x}}\right]^T \tag{204}$$

This simplifies to

$$\dot{\boldsymbol{\lambda}}_x = -\left(\frac{\partial \boldsymbol{F}}{\partial \boldsymbol{x}}\right)\boldsymbol{u}\boldsymbol{\lambda}_x - \left(\frac{\partial \boldsymbol{f}}{\partial \boldsymbol{x}}\right)^T \boldsymbol{\lambda}_x \tag{25}$$

For mass costate λ_m

$$\dot{\lambda}_m = -\frac{\partial H}{\partial m} = \frac{T_{\max}}{m^2}\boldsymbol{\lambda}_x^T \boldsymbol{F}\left(\boldsymbol{x},t\right)\boldsymbol{u} \tag{26}$$

A meticulous derivation of the Euler-Lagrange equations can be found in (Kechichia 1996).

From Pontryagin's Maximum Principle, the terminal condition for the mass costate is

$$\lambda_m\left(t_f\right) = \frac{\partial \Phi}{\partial m\left(t_f\right)} + \boldsymbol{\Lambda}^T \min_{\boldsymbol{u}\in U} = \left[\left(\boldsymbol{\lambda}_{\mathbf{x}}^T \mathbf{F}\left(x,t\right) - \frac{\lambda_m m}{I_{sp} g_0}\right)\boldsymbol{u}\right] \tag{27}$$

where Φ is the terminal cost, ψ is the terminal constraint, and $\boldsymbol{\Lambda}$ is a Lagrange multiplier vector. For free-final-mass problems, ψ it is independent of $m\left(t_f\right)$, so $\partial\psi/\partial m\left(t_f\right) = 0$.

Since $\Phi = 0$, we have

$$\lambda_m\left(t_f\right) = 0 \tag{28}$$

Following Pontryagin's maximum principle, the optimal controller $\mathbf{u}^*$ is determined by

minimizing the Hamiltonian. Referring to Eq. (19), this implies that $\mathbf{u}^*$ satisfies the following condition

$$\min_{\mathbf{u}\in U}\left(\left|\mathbf{F}(x,t)^T\boldsymbol{\lambda}_{\mathbf{x}}\right|\cos\alpha-\frac{\lambda_m m}{I_{sp}g_0}\right)\boldsymbol{u} \tag{29}$$

where $U=\{\boldsymbol{u}:|\boldsymbol{u}|\le 1\}$ is the admissible control set represented by $\alpha=\angle\mathbf{F}(x,\widehat{t)^T}\boldsymbol{\lambda_x},\boldsymbol{u}$ (the angle between the vectors). The optimal controller $\boldsymbol{u}$ is determined in accordance with Pontryagin's Maximum Principle. Since $\boldsymbol{\lambda}_{\mathbf{x}}^T\boldsymbol{f}$ is independent of $\boldsymbol{u}$ in Eq. (2), the minimization simplifies to

$$\min_{\boldsymbol{u}\in U}=\left[\left(\boldsymbol{\lambda}_{\mathbf{x}}^T\mathbf{F}(x,t)-\frac{\lambda_m m}{I_{sp}g_0}\right)\boldsymbol{u}\right] \tag{30}$$

Let $\Upsilon=\mathbf{F}(x,t)^T\boldsymbol{\lambda}_x$, then the term becomes

$$\min_{\boldsymbol{u}\in U}=\left[\left(\boldsymbol{\Upsilon}^T\boldsymbol{u}-\frac{\lambda_m m}{I_{sp}g_0}\right)\boldsymbol{u}\right] \tag{31}$$

Using $\Upsilon^T\boldsymbol{u}=|\Upsilon||\boldsymbol{u}|\cos\alpha$, where α is the angle between Υ and $\boldsymbol{u}$. Thus

$$\min_{\boldsymbol{u}\in U}=\left[|\boldsymbol{\Upsilon}|\cos\alpha-\frac{\lambda_m m}{I_{sp}g_0}\right]\boldsymbol{u}, \qquad |\boldsymbol{u}|\le 1 \tag{32}$$

The Hamiltonian is minimized when $\cos\alpha=-1$. Thus

$$\begin{cases}\boldsymbol{u}^*=-\dfrac{\boldsymbol{\Upsilon}}{|\boldsymbol{\Upsilon}|}=-\dfrac{\mathbf{F}(x,t)^T\boldsymbol{\lambda}_x}{\left|\mathbf{F}(x,t)^T\boldsymbol{\lambda}_x\right|}, & \left|\mathbf{F}(x,t)^T\boldsymbol{\lambda}_x\right|\neq 0\\ \boldsymbol{u}^*=\mathbf{0}, & \left|\mathbf{F}(x,t)^T\boldsymbol{\lambda}_x\right|=0\end{cases} \tag{33}$$

If $\Upsilon=0$, Eq. (22) reduces to

$$H=-\lambda_m\frac{T_{\max}}{I_{sp}g_0}|\boldsymbol{u}| \tag{34}$$

6. Optimal thrust integration for semi-major axis and eccentricity variation

By computing the first partial derivatives of the Eq. (2) with respect to the thrust angles, we can determine the optimal thrust angle values that maximize the rate of change of certain orbital parameters as a function of true anomaly. For instance, taking the derivative of the second equation (Eq. (2)) with respect to the out-of-plane thrust angle β,

$$\begin{aligned}\frac{\partial}{\partial\beta}\frac{\partial e}{dt}&=\frac{\partial}{\partial\beta}\left(\frac{1}{h}\chi\cos(\beta)\left(p\sin(\theta)\sin(\alpha)+\left((p+r)\cos(\theta)+re\right)\cos(\alpha)\right)\right)\\&=\frac{-1}{h}\chi\sin(\beta)\left(p\sin(\theta)\sin(\alpha)+\left((p+r)\cos(\theta)+re\right)\cos(\alpha)\right)\end{aligned} \tag{35}$$

For maximum $\frac{de}{dt}$ set $\frac{\partial}{\partial\beta}\frac{de}{dt} = 0$

To get $\frac{\partial}{\partial\beta}\frac{de}{dt} = 0$ the first part must be zero $-\frac{1}{h}\chi\, sin(\beta)$ or the second part $\big(p\, sin(\theta)\, sin(\alpha) + \big((p+r)\, cos(\theta) + re\big)\, cos(\alpha)\big)$

- For the $\frac{-1}{h}\chi\, sin(\beta) = 0 \rightarrow \beta = 0$, the thrust is purely in plane (planar thrusting).
- For $\big(p\, sin(\theta)\, sin(\alpha) + \big((p+r)\, cos(\theta) + re\big)\, cos(\alpha)\big) = 0$ which leads to $\frac{de}{dt} = 0$ which is not maximum.

Hence for maximum of $\frac{de}{dt}$ the thrust must be applied in the transverse or radial direction (planar thrusting), not normal to the plane $\beta = 0$ (planar thrusting).

The variation of the semi-major axis derived from Gauss's planetary equations simplified to

$$\frac{da}{dt} = \frac{2a^2\chi}{h}\left[e\sin\theta\sin\alpha_a^{opt} + \frac{p}{r}\cos\alpha_a^{opt}\right] \tag{36}$$

The in-plane thrust angle (α) for semi-major axis (a) adjustment is α_a^{opt} represented as

$$\alpha_a^{opt} = \arctan\left(\frac{e\sin\theta}{1+e\cos\theta}\right) \tag{37}$$

This angle ensures the thrust vector is aligned with the instantaneous velocity direction, maximizing the efficiency of semi-major axis changes.

Substitute the optimal thrust angle $(\boldsymbol{\alpha})$ into $\boldsymbol{da/dt}$

$$\frac{da}{dt} = \frac{2a^2\chi}{h}\left[\frac{e^2\sin^2\theta + \frac{p}{r}(1+e\cos\theta)}{\sqrt{e^2\sin^2\theta + (1+e\cos\theta)^2}}\right] \tag{38}$$

Since $p = a(1-e^2)$ and $r = \frac{p}{1+e\, cos\, \theta}$, the term $\frac{p}{r}$ reduces to $\frac{p}{r} = 1 + e\, cos\, \theta$

Thus, Eq. (28) becomes

$$\frac{da}{dt} = \frac{2a^2\chi}{h}\sqrt{e^2\sin^2\theta + (1+e\cos\theta)^2} \tag{39}$$

For circular orbits $(e = 0)$, this reduces to

$$\frac{da}{dt} = \frac{2a^2\chi}{h} \tag{40}$$

The optimal in-plane thrust angle for maximizing the rate of change of eccentricity is given by

$$\alpha_e^{opt} = \arctan\left(\frac{\sin\theta}{\cos\theta + \cos E}\right) \tag{41}$$

where E is the eccentric anomaly, and given by

$$E = \tan^{-1}\left(\frac{\sqrt{1-e^2}\sin(\theta)}{1+e\cos(\theta)}\right) \tag{42}$$

Table 1 The initial orbital parameters and satellite features for a LEO mission

Satellite/orbit property	Value
Semi-major axis (a)	6928 km
Eccentricity (e)	0.0505
Inclination (i)	53°
Right Ascension of Ascending Node (Ω)	0º
Argument of Periapsis (ω)	0°
True Anomaly (θ)	0°

Table 2 Specifications of the ion thruster

Specification	Value
Input power	30 dBW
Thrust	0.165 N
Specific impulse	3800 seconds
Mass flow rate	4.429×10-6 kg/s

Table 3 Specifications of the fuel tank

Specification	Value
Pressure	14,000 kPa
Volume	0.25 m^3
Temperature	323.15 K
Fuel density	800 kg/m^3
Fuel mass	3 kg
Maximum fuel mass	4 kg
Dry mass	200 kg

For the planar thrusting ($\beta = 0$), this simplifies to

$$\frac{de}{dt} = \frac{\chi}{h}\left[p\sin\theta\sin\alpha_e^{opt} + \left((p+r)\cos\theta + re \right)\cos\alpha_e^{opt} \right] \tag{43}$$

Final simplified form for near-circular orbits, this simplifies to

$$\frac{de}{dt} \approx \frac{3}{2}\frac{\chi\sqrt{a}}{\sqrt{\mu}} \tag{44}$$

where μ is the Earth gravitational parameter (3.986×10^{14} m^3/s^2). A summary of the relevant satellite parameters is provided in Table 1.

The power generated by the small spacecraft from internal sources is 30 dBW which is a constant power, and the power available from a power processing unit (*PPU*) is 0.90. The ion thruster is a versatile and reliable propulsion system that can operate in both sunlight and eclipse. It has a nominal input power of 30 dBW, producing 0.165 N of thrust at a specific impulse of 3800 seconds. This means that the thruster can produce a significant amount of thrust with a relatively small amount of propellant, making it ideal for long-duration missions. The mass flow rate of 4.429×10^{-6} kg/s is also very low, which means that the thruster can operate for a long time without

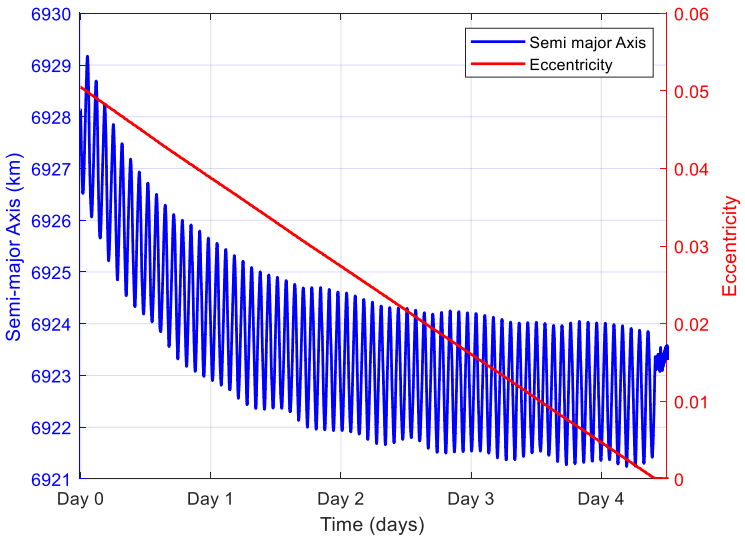

Fig. 3 Time evolution of mean semi-major axis and eccentricity

consuming much propellant. Table 2 presents the specifications of the ion thruster.

The spacecraft's fuel tank is a crucial component that supplies the fuel necessary to power the spacecraft's engines. It is constructed from a lightweight and strong material, such as aluminium or carbon fibre. It is designed to withstand the high pressures and temperatures encountered during launch and ascent.

The tank operates at a pressure of 14,000 kPa, has a volume of 0.25 m^3, a temperature of 323.15 K, a fuel density of 800 kg/m^3, a fuel mass of 3 kg, and a maximum fuel capacity of 4 kg. The specifications of the fuel tank are listed in Table 3.

7. Simulation of optimal control strategy

In this simulation, we use optimal control theory to minimize a cost function that reduces the spacecraft's velocity increments while tracking the evolution of the orbit's semi-major axis over time. We implemented a low-thrust, continuous acceleration strategy and analyzed the orbital evolution over multiple orbits. The simulation was conducted using Systems Tool Kit (STK v11.4.1), specifically its Astrogator module provided by Analytical Graphics Inc. We employed a high-precision orbit propagator that uses numerical integration of differential equations of motion to generate ephemeris data. It is worth noting that most previous studies (Herman and Spencer 2002, Kechichian 1997, Wang *et al.* 2021, Taheri *et al.* 2017, Han *et al.* 2020, Haberkorn and Gergaud 2004) ignore these perturbative effects when addressing low-thrust orbit circularization problems.

Fig. 3 illustrates the temporal evolution of the semi-major axis and eccentricity of the spacecraft's orbit during a finite maneuver executed using continuous low-thrust propulsion. Over five days of circularization, the trajectory exhibits a smooth and progressive decrease in the semi-major axis, reflecting a controlled reduction in orbital energy. Simultaneously, the orbital eccentricity steadily decreases toward near-zero, confirming the achievement of orbit

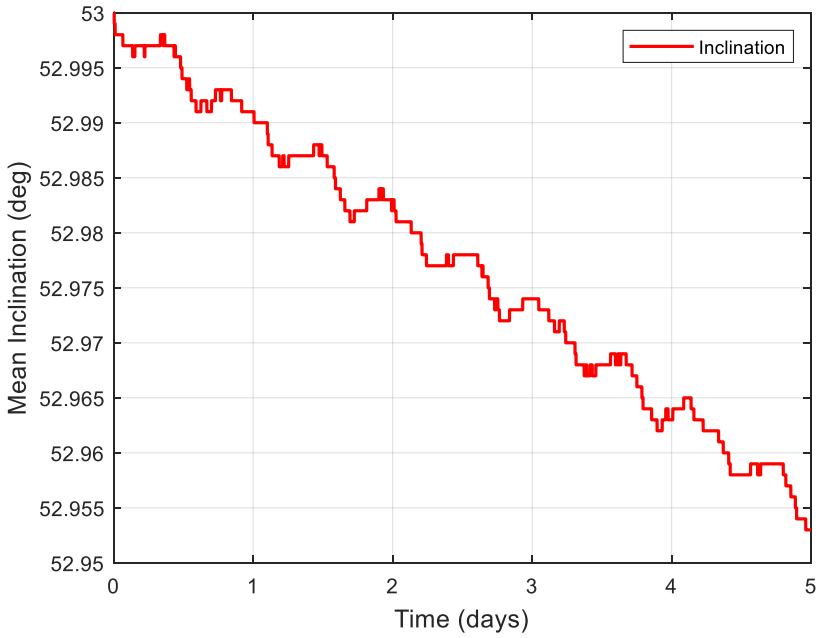

Fig. 4 Time evolution of mean inclination

circularization.

This strategy validates the performance of the applied optimal control approach, which continuously adjusts the thrust direction to achieve dual objectives: orbital contraction and damping of eccentricity. The continuous evolution of the trajectory is typical of finite low-thrust maneuvers and demonstrates precise trajectory shaping with consistent tracking performance by the control system.

The mean inclination of the satellite was tracked during the 5-day low-thrust orbit circularization maneuver to assess the stability of the orbital plane. As shown in Fig. 4, the inclination remained nearly constant, varying only slightly between 52.997° and 53.000°.

This minimal variation indicates that the applied thrusting strategy was mainly effective in adjusting the orbit's shape (i.e., reducing eccentricity) without significantly perturbing the inclination.

The evolution of the satellite's apogee and perigee altitudes over the 5-day low-thrust maneuver is shown in Fig. 5. Initially, a significant disparity exists between apogee (~900 km) and perigee (~200 km), indicating a highly elliptical orbit.

As the maneuver progresses, the altitudes converge, confirming the successful transition toward a circular orbit. The consistent decrease in apogee and increase in perigee altitude indicate effective energy redistribution through sustained low-thrust propulsion. This behaviour aligns with the mission objective of achieving orbit circularization while keeping altitude control and fuel efficiency.

The evolution of the Mean Right Ascension of the Ascending Node (RAAN) was analyzed over the 5-day low-thrust circularization maneuver. The results, shown in Figure 6, indicate a smooth and gradual decrease in RAAN from approximately 0° to 358°. This behavior confirms that the applied thrust was primarily in the orbital plane, with negligible out-of-plane thrust

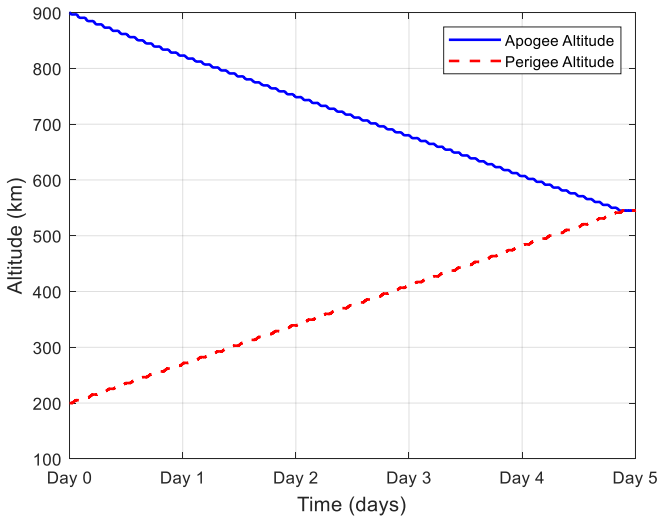

Fig. 5 Time evolution of mean apogee and perigee altitudes

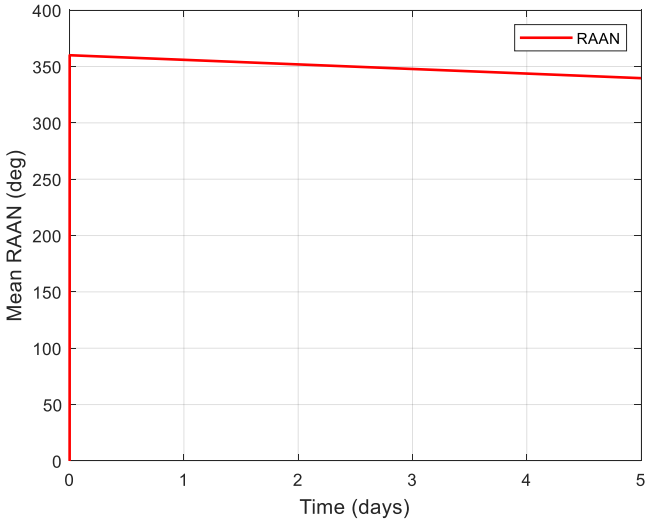

Fig. 6 Time evolution of mean RAAN

components. The absence of significant oscillations or discontinuities in the RAAN profile suggests high control precision and accurate thrust vector alignment. Maintaining this level of RAAN stability is crucial for missions that require precise orbital plane alignment and long-term ground track repeatability.

The Mean Anomaly was tracked throughout the low-thrust maneuver to assess the satellite's position along its orbit. The mean anomaly shows a consistent and nearly linear increase over the course of the simulation, ranging from 0° to approximately 360°, completing multiple full orbital revolutions.

This consistent progression confirms the stable orbital motion of the satellite under continuous low-thrust propulsion. The steady increase of the anomaly indicates well-coordinated energy

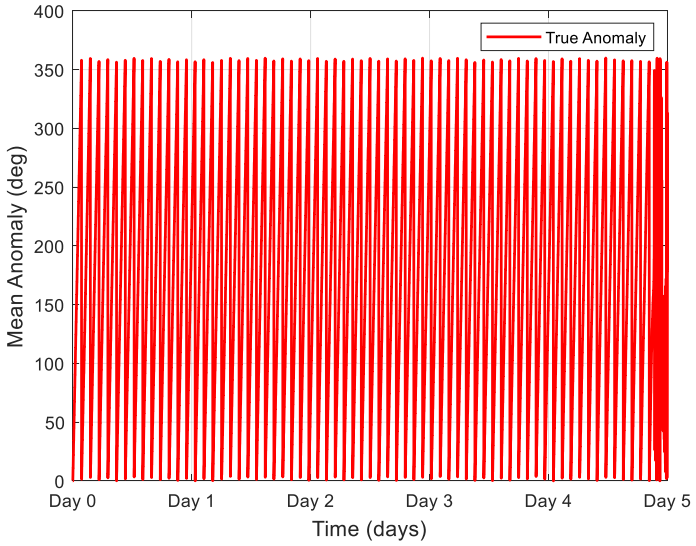

Fig. 7 Time evolution of mean anomaly

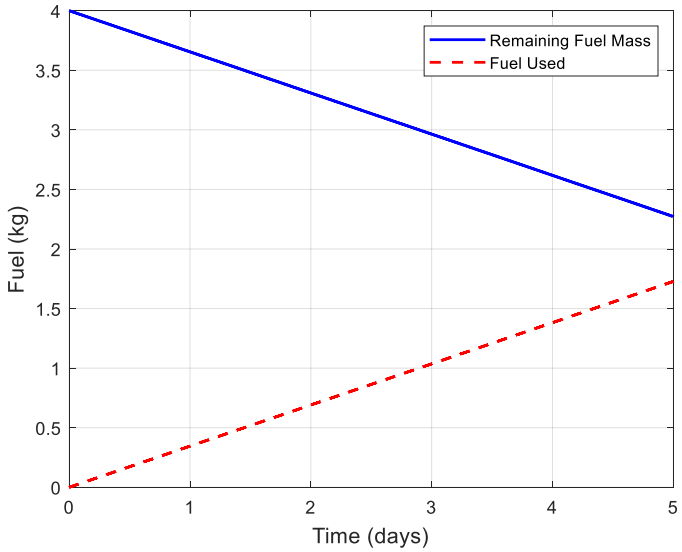

Fig. 8 Fuel mass and fuel used over time

management and burn timing, which are crucial for achieving effective orbit circularization.

Fig. 8 depicts the fuel mass and fuel consumption over time. Initially, fuel usage is low, but it gradually rises as the spacecraft advances through its low-thrust maneuver. In the initial phase, the fuel consumption increases as the spacecraft adjusts its orbit. Once the orbital parameters near their target values, the required thrust and consequently the fuel consumption rate decline. The total fuel utilized reaches approximately 1.44 kg over five days, indicating highly efficient propellant use.

The smooth and steadily increasing fuel consumption profile reflects stable and continuous

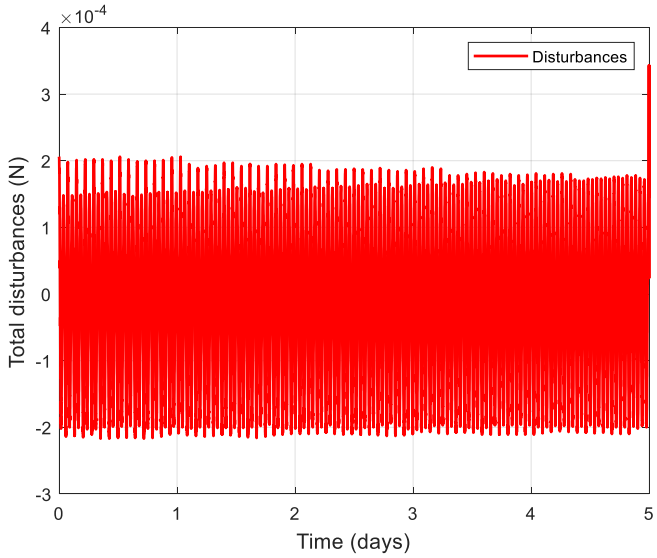

Fig. 9 The total disturbances over time

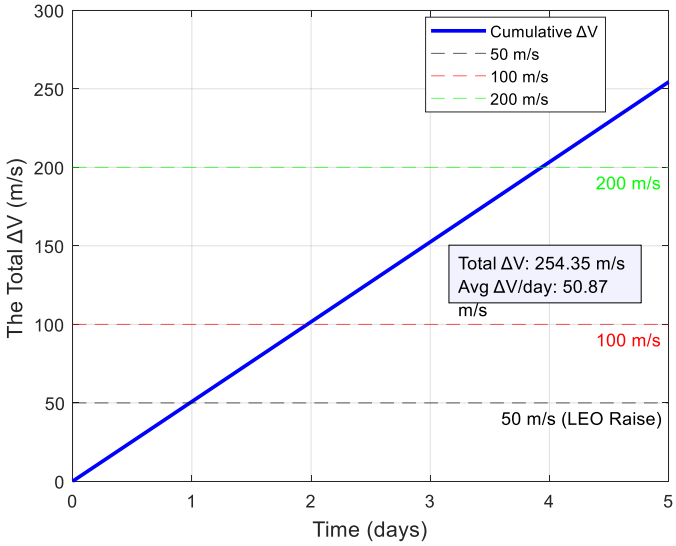

Fig. 10 Delta-v requirements for spacecraft maneuvers

thrusting, characteristic of electric propulsion. This affirms the effectiveness of the applied optimal control approach in achieving both orbital circularization and eccentricity damping with minimal propellant consumption, making it ideally suited for long-duration, fuel-sensitive missions.

The Mean perturbation was tracked over the 5-day simulation to assess the effectiveness of orbit circularization under the influence of environmental and dynamical disturbances affecting the satellite's trajectory. As shown in Fig. 9, the perturbation remained relatively stable throughout the maneuver, indicating variation and confirming that the orbit was dynamically well-controlled. The simulation environment included all relevant perturbative forces as configured in the STK HPOP

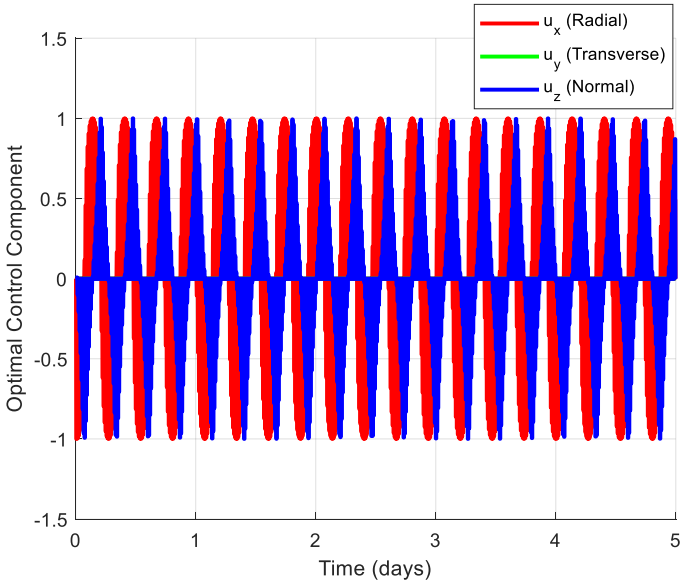

Fig. 11 Optimal control vector $u(t)$ in RTN frame (first 5 days)

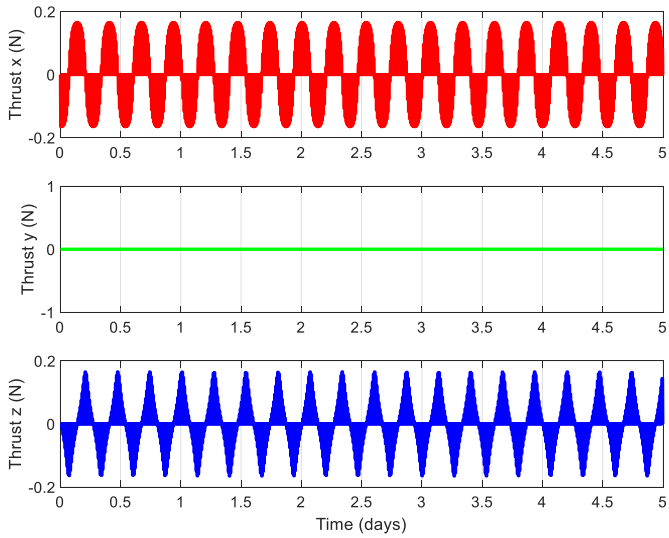

Fig. 12 Optimal control vector $u(t)$ in RTN frame (first 5 days)

model. A perturbation tolerance of around 10^{-4} is a crucial parameter that can significantly impact the fidelity of orbit design and long-term stability. The consistency observed in the perturbation rate confirms the accuracy of the thrust vector orientation and emphasises the robustness of the overall orbital design and maneuver strategy.

Fig. 10 shows the total Delta-V achieved during the 5-day low-thrust orbit circularisation manoeuvre. The Delta-V profile exhibits a smooth, steady increase, typical of electric propulsion systems operating under a continuous low-thrust mode. By the end of the manoeuvre,

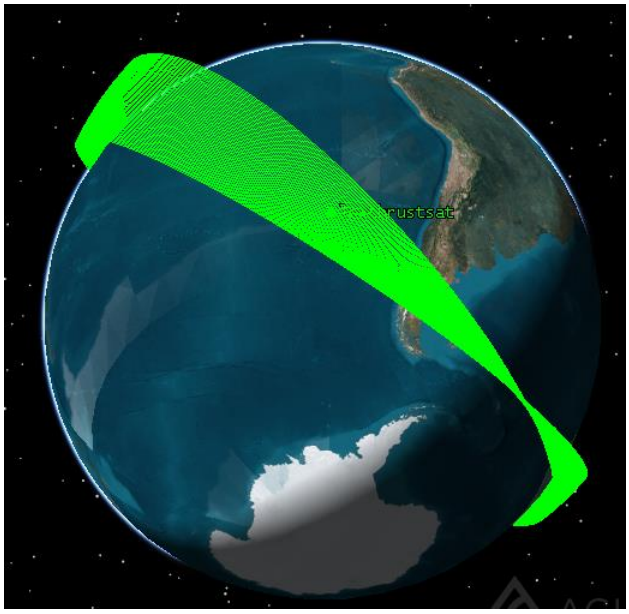

Fig. 12 The optimal trajectory of the satellite

approximately 254.35 m/s of Delta-V was applied. The average rate of Delta-V was 50.87 m/s per day, confirming consistent acceleration in line with the mission's orbit-raising objectives. The fuel consumption during the manoeuvre was 1.44 kg, demonstrating highly efficient propulsion performance.

Fig. 11 shows how the optimal control vector in the RTN frame changes over the first five days of simulation. The control vector is normalised (i.e., $|\boldsymbol{u}(\boldsymbol{t})| = \mathbf{1}$, (Eq. (34))), indicating the optimal thrust direction at each time step under Pontryagin's Maximum Principle. Each component represents the normalized projection of the thrust direction along the respective RTN axis. The figure confirms that the control law continuously adjusts the thrust direction to guide the spacecraft along its optimal trajectory. Notably, the components display smooth, bounded variations, reflecting the gradual attitude adjustments needed for orbit correction during the manoeuvre.

Fig. 12 shows the time history of the thrust vector components in the RTN frame during the first five days of the mission. Each subplot depicts one directional component of the applied thrust in Newtons: radial (x), transverse (y), and normal (z).

The thrust profiles demonstrate how the propulsion system dynamically adapts to optimise the spacecraft's trajectory. Smooth and steady variations in each component show an efficiently controlled low-thrust manoeuvre strategy, where the thrust direction shifts over time in response to the orbital state and control objectives. The plots verify that thrust is not applied constantly in a single direction but is instead distributed among the RTN components in a coordinated way to achieve gradual orbit correction.

Fig. 12 illustrates the optimal transfer trajectory. This solution has been obtained with the revolution number N=2167. This is particularly important for long-duration missions, as it can significantly extend the spacecraft's lifespan. To conclude this study, the manoeuvre summary report indicates that the circular order sequence was initiated every 180 seconds.

8. Conclusions

This study effectively demonstrated the feasibility and efficiency of using low-thrust electric propulsion for orbit circularisation and refinement of orbital elements in small satellites. Through a combination of analytical modelling and high-fidelity numerical simulations using STK Astrogator's HPOP, we validated the continuous-thrust manoeuvre over a 5-day mission profile. The Key orbital parameters, including mean semi-major axis, eccentricity, inclination, RAAN, and mean anomaly, were tracked and analysed. The eccentricity was reduced steadily to near-zero, indicating successful circularisation, while the semi-major axis was gradually decreased under well-controlled thrusting. The RAAN and inclination remained stable, confirming dynamic orbital stability under the influence of modelled perturbations.

A total Delta-V of 254.35 m/s was delivered with a corresponding fuel consumption of only 1.728 kg, demonstrating the excellent efficiency characteristic of electric propulsion. Fuel usage followed a low and predictable trend, reinforcing the stability and alignment of the long-duration thrust profile with the thrust vector design. These results confirm the effectiveness and robustness of low-thrust strategies in LEO and similar regimes, achieving both fuel-efficient and precise orbital manoeuvring.

Future work will focus on incorporating variable-specific impulse engines, modelling power constraints during eclipse periods, and integrating multi-objective optimisation techniques to balance time, fuel, and mission flexibility. Additionally, extending these techniques to interplanetary trajectory design could further expand the application domain of low-thrust electric propulsion.

Acknowledgments

We would like to thank the Algerian Space Agency for their technical support and for providing us with a license of the STK AGI software. This software has been invaluable in our research on low-thrust circularization and its ap-plication to low-Earth orbit missions. We would also like to thank Prof. Han Chao from Beihang University.

References

Analytical Graphics, Inc. (AGI) (2008), Satellite Tool Kit (STK). Available at: www.agi.com.

Battin, R.H. (1999), *An Introduction to the Mathematics and Methods of Astrodynamics*, Aiaa.

Betancourt, M.L.R., Bögela, E., Collier-Wrighta, M., Wilcoxa, J.L. and Kaplan, P.A. (2021), "Comparative overview of nuclear electric propulsion programs and concepts", *IAC-21*, 7.

Betts, J.T. and Erb, S.O. (2003), "Optimal low thrust trajectories to the moon", *SIAM J. Appl. Dyn. Syst.*, **2**(2), 144-170. https://doi.org/10.1137/S1111111102409080.

Casalino, L. and Colasurdo, G. (2007), "Improved Edelbaum's approach to optimize low earth/geostationary orbits low-thrust transfers", *J. Guid. Control Dyna.*, **30**(5), 1504-1511. https://doi.org/10.2514/1.28694.

Conway, B.A. (2012), "A survey of methods available for the numerical optimization of continuous dynamic systems", *J. Optim. Theor. Appl.*, **152**(2), 271-306. https://doi.org/10.1007/s10957-011-9918-z.

Enright, P.J. and Conway, B.A. (1992), "Discrete approximations to optimal trajectories using direct transcription and nonlinear programming", *J. Guid. Control Dyn.*, **15**(4), 994-1002. https://doi.org/10.2514/3.20934.

Haberkorn, T., Martinon, P. and Gergaud, J. (2004), "Low thrust minimum-fuel orbital transfer: a homotopic approach", *J. Guid. Control Dyn.*, **27**(6), 1046-1060. https://doi.org/10.2514/1.4022.

Han, C., Wang, Y., Chen, H., Sun, X., Sun, Y. and Li, J. (2020), "Practical low-thrust geostationary orbit transfer guidance via linearized state equations", *J. Guid. Control Dyn.*, **43**(3), 620-627. https://doi.org/10.2514/1.G004692

Herman, A.L. and Spencer, D.B. (2002), "Optimal low-thrust earth-orbit transfers using higher-order collocation methods", *J. Guid. Control Dyn.*, **25**(1), 40-47. https://doi.org/10.2514/2.4873.

Kechichian, J.A. (1996), "Optimal low-thrust rendezvous using equinoctial orbit elements", *Acta Astronautica*, **38**(1), 1-14. https://doi.org/10.1016/0094-5765(95)00121-2.

Kechichian, J.A. (1997), "Optimal low-earth-orbit-geostationary-earth-orbit intermediate acceleration orbit transfer", *J. Guid. Control Dyn.*, **20**(4), 803-811. https://doi.org/10.2514/2.4116.

Kéchichian, J.A. (2017), "Mathematics of attitude-constrained optimal low-thrust orbit transfer", *Aerotecnica Missili & Spazio*, **96**(4), 180-194. https://doi.org/10.1007/BF03404753.

Krejci, D. and Lozano, P. (2018), "Space propulsion technology for small spacecraft", *Proc. IEEE*, **106**(3), 362-378. https://doi.org/10.1109/JPROC.2017.2778747.

Ma, J., Wen, C. and Zhang, C. (2021), "Practical optimization of low-thrust minimum-time orbital rendezvous in sun-synchronous orbits", *Comput. Model. Eng. Sci.*, **126**(2), 617-644. https://doi.org/10.32604/cmes.2021.014474.

Manzella, D. (2007), "Low cost electric propulsion thruster for deep space robotic missions", *2007 NASA Science Technology Conference*, 07-0116.

Marcuccio, S., Pergola, P., Gregucci, S. and Andrenucci, M. (2015), "Low-thrust propulsion systems for small satellites", *Proceeding of the 66th International Astronautical Congress*, International Astronautical Federation.

Miao, X., Zhang, H., Wang, Q., Xia, Y. and Sun, W. (2022), "Optimum design of nuclear electric propulsion spacecraft for deep space exploration", *Energy Report.*, **8**, 9629-9641. https://doi.org/10.1016/j.egyr.2022.07.146.

Miller, S., Walker, M.L., Agolli, J. and Dankanich, J. (2021), "Survey and performance evaluation of smallsatellite propulsion technologies", *J. Spacecraft Rocket.*, **58**(1), 222-231. https://doi.org/10.2514/1.A34774

Misuri, T., Albertoni, R., Ducci, C., Waldvogel, B., Appel, L., Eytan, R., ... & Di Cara, D. (2015), "MEPS: A low power electric propulsion system for small satellites", *Proceedings of the 10th IAA Symposium on Small Satellites for Earth Observation*, 20-24.

Morante, D., Sanjurjo Rivo, M. and Soler, M. (2021), "A survey on low-thrust trajectory optimization approaches", *Aerosp.*, **8**(3), 88. https://doi.org/10.3390/aerospace8030088.

O'Reilly, D., Herdrich, G. and Kavanagh, D.F. (2021), "Electric propulsion methods for small satellites: A review", *Aerosp.*, **8**(1), 22. https://doi.org/10.3390/aerospace8010022.

Petropoulos, A. (2004), "Low-thrust orbit transfers using candidate Lyapunov functions with a mechanism for coasting", *AIAA/AAS Astrodynamics Specialist Conference and Exhibit*, 5089. https://doi.org/10.2514/6.2004-5089.

Petropoulos, A.E. (2003), "Simple control laws for low-thrust orbit transfers".

Rao, A.V. (2009), "A survey of numerical methods for optimal control", *Adv. Astronaut. Sci.*, **135**(1), 497-528.

Rayman, M.D., Chadbourne, P.A., Culwell, J.S. and Williams, S.N. (1999), "Mission design for deep space 1: A low-thrust technology validation mission", *Acta Astronautica*, **45**(4-9), 381-388. https://doi.org/10.1016/S0094-5765(99)00157-5.

Reiter, J.A. and Spencer, D.B. (2016), "An analytical solution to quick-response collision avoidance maneuvers in low earth orbit", *AIAA 26th AAS/AIAA Space Flight Mechanics Meeting*, 1-11.

Rosa Sentinella, M. and Casalino, L. (2006), "Genetic algorithm and indirect method coupling for low-thrust trajectory optimization", *42nd AIAA/ASME/SAE/ASEE Joint Propulsion Conference & Exhibit*, 4468. https://doi.org/10.2514/6.2006-4468.

Staniscia, G. (2011), "Development of a low earth orbit mission preliminary analysis tool".

Taheri, E., Li, N.I. and Kolmanovsky, I. (2017), "Co-state initialization for the minimum-time low-thrust trajectory optimization", *Adv. Space Res.*, **59**(9), 2360-2373. https://doi.org/10.1016/j.asr.2017.02.010.

Vallado, D.A. (2001), *Fundamentals of Astrodynamics and Applications*, Vol. 12, Springer Science & Business Media.

Vavrina, M. and Howell, K. (2009), "Multiobjective optimization of low-thrust trajectories using a genetic algorithm hybrid", *AAS/AIAA Space Flight Mechanics Meeting*, 09-141.

Wang, Y., Han, C. and Sun, X. (2021), "Optimization of low-thrust Earth-orbit transfers using the vectorial orbital elements", *Aerosp. Sci. Technol.*, **112**, 106614. https://doi.org/10.1016/j.ast.2021.106614.

Yue, X., Yang, Y. and Geng, Z. (2009), "Continuous low-thrust time-optimal orbital maneuver", *Proceedings of the 48h IEEE Conference on Decision and Control (CDC) held jointly with 2009 28th Chinese Control Conference*, 1457-1462. https://doi.org/10.1109/CDC.2009.5399622.

AP